Atmos. Chem. Phys. Discuss., 9, 20739–20763, 2009
www.atmos-chem-phys-discuss.net/9/20739/2009/

Atmospheric Chemistry and Physics Discussions

This discussion paper is/has been under review for the journal *Atmospheric Chemistry and Physics (ACP)*. Please refer to the corresponding final paper in *ACP* if available.

Scanning electron microscopy and molecular dynamics of surfaces of growing and ablating hexagonal ice crystals

W. C. Pfalzgraff, R. M. Hulscher, and S. P. Neshyba

University of Puget Sound, Tacoma, Washington, 98416, USA

Received: 10 August 2009 – Accepted: 21 August 2009 – Published: 1 October 2009

Correspondence to: S. P. Neshyba (nesh@pugetsound.edu)

Published by Copernicus Publications on behalf of the European Geosciences Union.

Abstract

Optical properties of cirrus ice clouds play an important role in regulating Earth's radiative balance. It has been hypothesized that the surfaces of cirrus ice crystals may be characterized by mesoscopic (micrometer-scale) texturing, or roughness, in order to explain discrepancies between theoretical and observed light-scattering properties. Here, we present the first clearly resolved observations of surfaces of hexagonal ice crystals, using variable-pressure scanning electron microscopy. During growth conditions, the ice surface develops trans-prismatic strands, separated from one another by distances of 5–10 μm. These strands become more pronounced during ablation, and exhibit a wider range of separations. Under re-growth conditions, faceting is re-established initially at prismatic edges. Molecular dynamics studies of a free-standing ice I_h nanocolumn showed no trans-prismatic strands at the atomistic level, suggesting that these strands originate at a spatial scale greater than 10 nm. The observed surface roughness could be used to construct more realistic representations of cirrus clouds in climate models, and constrain theories of ice crystal growth and ablation.

1 Introduction

One objective of cloud microphysics is to represent the morphology of cirrus cloud crystals well enough that their optical properties are faithfully represented in climate models (Stephens et al., 1990). On a spatial scale of 10–100 μm, this objective has been met with considerable success. We know, for example, that ice crystals in midlattitude cirrus clouds have relatively spherical shapes near the top, and more pristine hexagonal prisms at midlevel (Heymsfield and Iaquinta, 2000). We know how these varying morphologies affect the optical properties of cloud particles, through parameters such as the asymmetry parameter. For example, equidimensional hexagonal prisms have a smaller asymmetry parameter than columns or plates of a similar size, hence clouds comprised of the former will backscatter photons more effectively (Neshyba et al., 2003;

Yang et al., 2008a).

Morphological properties of cirrus ice crystals on a mesoscopic (micrometer-level) scale are less well characterized. Evidence for some kind of mesoscopic structure has emerged from in situ studies of cirrus clouds, which have revealed a distribution of asymmetry parameters whose mean is smaller than can be accounted for by crystal habit alone (Gerber et al., 2000; Lampert et al., 2009). To account for the discrepancy, a mesoscopic roughness hypothesis has been invoked, in which surfaces are modified to simulate roughness (Garrett, 2008). This modification works in the desired direction (to lower asymmetry parameters) (Yang and Liou, 1998; Ulanowski et al., 2006), but now a new problem arises: there is no way to predict the degree of roughness. Without an independent, experimental way to characterize mescoscopic surface roughness of ice crystals, the ability of the rough-surface hypothesis to offer new predictive capability is very limited.

Are the surfaces of cirrus ice crystals mesoscopically rough? Optical micrographs of cirrus ice crystals and snowflakes have suggested the presence of texturing (Yang et al., 2008a; Bailey and Hallett, 2004), but interpretation is hampered by resolution limits inherent to optical microscopy. Scanning electron microscopy (SEM) has long been recognized as an attractive alternative for observing ice morphology (Cross, 1968; Rango et al., 2000; Erbe et al., 2003), because of its resolution and depth of field. However, the high vacuum conditions and coating procedures usually employed to prepare samples do not permit observation of growth dynamics. Recently, variable pressure SEM (VP-SEM) has been used to study crystals grown inside the chamber of the instrument and imaged as they grew (Zimmerman et al., 2007; Cartwright et al., 2008). However, surface features have remained unexplored with this technique because the crystals grown were small (tens of micrometers in diameter), and the increase in current density for magnifications above 1000x caused melting or evaporation of the ice.

In principle, theories of ice crystal growth could help settle the question posed above. For example, some ice growth models invoke assumptions about mesoscopic surface structure (Gravner and Griffeath, 2009; Wood et al., 2001), but these theories do not

predict the scale of such roughness, which is essential information for optical scattering purposes. Molecular dynamics (MD) may eventually provide insight into the molecular-level processes connected to surface morphology, despite limitations of scale (simulation of a few thousand water molecules over a few milliseconds can take weeks).

The foregoing suggests that high-quality images of the surfaces of cirrus ice, or cirrus ice analogues, would be useful for constraining theories of crystal growth and ablation, as well as for climatological and remote-sensing purposes. Here, we present VP-SEM micrographs showing surface features associated with growth and ablation of hexagonal ice prisms growing on a cold copper substrate. Our technique creates water vapor supersaturations as high as 500% at the examination stage, which allows ice crystals to grow to several hundred micrometers in diameter. On these larger crystals, magnifications of 400–700x reveal surface properties not previously seen, including dynamic ruffled textures that accompany growth, ablation, and re-growth. We also present results of molecular dynamics (MD) simulations of a free-floating hexagonal ice prism, undertaken in the hope that atomistic counterparts to observed structures may provide insight into their microscopic origins.

2 Methods

2.1 Growth, ablation, and imaging of ice hexagons in an SEM chamber

Micrographs were obtained using a Hitachi S-3400N VP-SEM equipped with a backscattered electron detector and an accelerating voltage of 10–15 kV. A rough-cut copper specimen stub mounted on an examination stage was cooled with a Deben Ultra Coolstage MK3 version Peltier cooling element. Water vapor was introduced by placing a metal reservoir with ∼4 mL of de-ionized liquid water inside the VP-SEM chamber. Once an operating pressure of 50 Pa was reached, the Peltier cooling system was set to 228 K. The examination stage was then monitored at low magnification (∼20x) until the first ice crystals were evident.

Growth conditions at the examination stage existed as long as the temperature was sufficiently low and there remained water in the reservoir. Conversely, ablation conditions could be induced by raising the temperature of the cold stage, or by allowing the reservoir in the chamber to go dry. Structural changes that attend growth and ablation could thereby be observed for the same crystal.

2.2 Molecular dynamics of a free-standing nanocolumn and a prismatic slab

A rectangular volume of ice I_h, comprised of thirty ice bilayers of 280 molecules each (totaling of 8400 molecules), was initially constructed according to the proton disordering algorithm of (Buch et al., 1998). The orientation of this volume was such that the basal surface lay perpendicular to the z-axis, and the prismatic surface lay perpendicular to the y-axis. Initial dimensions of the crystal were 4.46, 5.45, and 11.00 nm in the x, y, and z directions. For the first part of the MD simulation, box dimensions were extended in the x and y dimensions to 7.5 and 8.0 nm, respectively, for 20 ns, to allow the system to anneal to an approximately hexagonal cross section (after Pereyra and Carignano, 2009). Subsequently, the simulation box in the z direction was extended to 14.4 nm, thereby exposing the basal surfaces to vacuum as well. Integration of classical equations of motion was performed by Gromacs molecular dynamics software (Lindahl et al., 2001), with rigid molecules interacting according to a 6-site intermolecular potential (Nada and van der Eerden, 2003), constant NVT conditions, a 1-femtosecond integration step, Berendsen temperature coupling with a time constant of 0.1 ps, and a temperature of 250 K. For long-range Coulomb interactions, particle-mesh Ewald summation was used with a relative tolerance of $1\text{x}10^{-5}$, 4th order cubic interpolation, and a Fourier spacing parameter of 0.12. For Van der Waals interactions, a cut-off radius of 0.07 nm was used. Angular and linear momentum of the system as a whole were removed at intervals of 50 femtoseconds. This system is referred to hereinafter as a free-standing nanocolumn.

A second ice I_h system was a slab of hexagonal ice composed of 1280 water molecules, initially measuring 3.59, 3.11, and 3.67 nm in the x, y, and z directions,

but with the box dimension in the *y* direction extended to 5.0 nm to simulate exposure of the prismatic surface to vacuum. Other computational parameters were as described above, except that only linear (not angular) momentum of the system as a whole was removed. This system is referred to hereinafter as a prismatic slab.

At the temperatures considered here, ice surfaces exposed to air develop a quasi-liquid layer. For the purpose of visualizing only the underlying ice, quasi-liquid molecules were defined as those with an average of 3.8 or fewer hydrogen bonds over a 1 ns period; this is a stricter criterion than that used by Carignano et al. (2005), who used a cutoff value of 3.3 hydrogen bonds. VMD imaging software was used to visualize simulation results in such a way that quasiliquid molecules were rendered differently from underlying ice (Humphrey et al., 1996).

Vapor pressures associated with ice surfaces exposed to vacuum were calculated according to a modified Hertz-Knudsen formula (Saito, 1996),

$$P_{\text{vap}} = R\sqrt{2k_B T\, m} \tag{1}$$

where T=250 K, k_B is Boltzmann's constant, m is the mass of a water molecule, and R is the departure rate of molecules to vacuum divided by the surface area of the simulated ice. The latter is given by $3.59\times3.67\times2=26.2\,\text{nm}^2$, where the factor of 2 accounts for exposure of two prismatic surfaces to vacuum. For the free-standing nanocolumn, the relevant area was taken to be that of a cylinder oriented in the z-direction, 11.00 nm in length, having a cross-sectional area equal to that of the initial rectangular volume ($4.46\times5.45\,\text{nm}^2$); the result was an area of $241\,\text{nm}^2$.

3 Results

3.1 SEM images

Crystals began to be visible on the examination stage typically 5–15 min after the beginning of an SEM session. Of the visible crystals, 20–50% were isolated hexagonal

prisms, the rest polycrystalline aggregates. In the first few minutes of growth, crystals usually grew too quickly to produce high-resolution images, although they could be monitored in real time at low resolution.

Figure 1, taken 12 min after initial ice formation was observed (and growth had slowed), shows two hexagonal crystals. The crystal on the left is more typical in that its prismatic surface is visible at a near-normal angle, and its basal facet is tilted away from the detector. The second crystal is atypical in that the basal facet faces the detector. Both crystals have another set of facets associated with each prismatic surface, designated here as prismatic pyramidal facets. These facets subtend an angle of $\sim 14^{\circ}$ with respect to the plane of the prismatic facet. During early, fast growth, crystals also display a non-faceted surface with conical symmetry (CNF surface). The CNF surface is small or not present in larger, slower-growing crystals. In the crystal on the right, the circular intersection between the basal facet and the CNF surface is evidence for the conical symmetry of the latter.

Figure 2 shows an isolated hexagonal crystal at an earlier growth stage. The first micrograph in the series was taken immediately after its presence was noticed (i.e. after nucleation on the copper specimen stub). The second micrograph was taken 32 s later, implying growth rates of 0.7 and $0.8\,\mu\mathrm{m\,s^{-1}}$ in the prismatic and basal facets, respectively.

Figure 3a and b are low-magnification views of a crystal under supersaturated (growth) and undersaturated (ablation) conditions, respectively. A ruffled pattern, comprised of what will be designated here as trans-prismatic strands, is evident in both, but the ablating crystal is much rougher overall. Although similar in certain respects, strands that appear under growth conditions are different dynamically and morphologically from strands that appear under ablation conditions, as described in more detail below. For this reason, it will be convenient to distinguish them as "growth strands" and "ablation strands".

Focusing first on growth strands, Fig. 3c–f are a series of higher-magnification micrographs of the same ice crystal as in Fig. 3a–b, taken under growth conditions (228 K),

at $\sim$30 s intervals. A prismatic edge appears at the bottom of each figure. Strands are clearly evident in these figures, separated from one another by 5–10 μm. Supplemented by real-time observations (not shown), these sequences suggest collective dynamics: originating near one prismatic edge, strand-ends often advanced together, forming a front; once the front came within a few tens of micrometers from the adjacent edge, it retreated, leaving a smooth surface immediately adjacent to the prismatic edge. This collective advance and retreat continued at irregular intervals of 20–40 s. Growth strands are present for a wide range of supersaturations; this sequence was taken about an hour into the experiment, which corresponded to a supersaturation of 100–200% (supersaturation calculations are described below).

Figure 3g–i are a series of higher-magnification micrographs of the same ice crystal, also taken at $\sim$30 s intervals, but under ablation conditions (250 K). Dynamically, ablation strands deepen first at the prismatic edge, and at indentations in the smooth prismatic surface away from the edge (marked in Fig. 3g). The deepening extends along the prismatic strands (Fig. 3g–i), eventually roughening nearly the entire prismatic surface (evident in Fig. 3b) (a remnant of the original faceted surface is evident in the middle of the facet). The result is that, unlike growth strands, ablation strands are roughest and deepest near the prismatic edge, and the overall texture of the ablated surface is rougher as well. Finally, it is striking that the prismatic edge remains clearly defined despite pronounced ablation.

On the prismatic pyramidal facet, ledges and terraces are evident under both growth and ablation conditions, suggesting that growth and ablation on these facets are not mediated by trans-prismatic strands but instead by the formation and ablation of ledges.

We turn next to the question of how previously ablated crystals recover when re-exposed to growth conditions. Figures 4a–d show an ablated crystal near a prismatic edge at 600x magnification, after returning the temperature of the examination stage to 228 K. The first visual cue that re-growth is occurring is the appearance of a short-lived, smooth, beveled surface along the remains of the prismatic edge (Fig. 4b), which quickly spreads to cover the rough texture along the ablated edge. Within minutes,

these smooth surfaces appear to define beveled precursor segments to a reforming prismatic edge, several of which are visible in Fig. 4c and d.

Figures 3e–h, taken approximately 90 s apart, demonstrate continued re-growth. Growth is clearly occurring because the crystal becomes wider and taller as the series progresses. The reconstruction of the smooth surface proceeds in a zipper-like fashion, moving up and to the right in the figure. We also note that the ablated area changes very little in this sequence. Trans-prismatic growth strands are visible on the smoother, re-grown part of the facet, and these strands exhibit collective dynamics like those in Fig. 3a. There are ledges in the area where the prismatic pyramidal facet is re-growing, which fade as the intersection of the prismatic pyramidal facet with the two prismatic facets reforms (Fig. 3e–f). The prismatic pyramidal facet itself appears to re-grow by formation of much larger ledges.

Figures 4i–l are a sequence of higher magnification views taken a few minutes later, still under re-growth conditions. Ablation strands are no longer evident on the prismatic facets. Indeed, the similarity between the structure and dynamics of this re-growing prismatic surface and those of Fig. 3a suggests identical growth mechanisms. This sequence further demonstrates that strand-mediated growth is not operative on other facet types; the prismatic pyramidal facet appears to re-grow by the formation of much larger ledges (20 μm wide and 5 μm deep).

Figure 5a shows temperatures at which prismatic surfaces were observed to change from growth to ablation patterns, obtained by taking the Peltier cooler through cycles of heating and cooling over the course of a single SEM session. These temperatures define a facet frost temperature, T_f, for the chamber. Figure 5b shows the supersaturation at the examination stage under normal viewing conditions, obtained by

$$\sigma = \left(\frac{P_{\text{vap}}(T_f)}{P_{\text{vap}}(T_s)} - 1 \right) \times 100 \qquad (2)$$

where T_s is the nominal temperature of the examination stage (228 K), and P_{vap} is given by (Buck, 1981). Values at the beginning of the session are extrapolated, since crystals

were not visible in the first 13 min. Since the total pressure in the SEM chamber was 50 Pa, the extrapolated value of P_{vap} indicates the SEM chamber initially contained 90% water vapor, and the supersaturation at the cold stage was nearly 500%.

3.2 Molecular dynamics simulations

Figure 6 shows the integrated oxygen atom number density of the free-standing nanocolumn as a function of distance along the crystallographic c-axis, for various times after exposure of basal surfaces to vacuum. The similarity of curves corresponding to 5 and 8 ns suggests the structure has converged. The potential energy over 14 ns of simulation time had a standard deviation of 0.06 kJ/mol, with a mean of −48.1 kJ/mole, indicating a stable configuration.

Figure 7a shows a configuration of the free-standing nanocolumn 4 ns after the exposure of basal surfaces to vacuum, with ice-like molecules rendered as solid shapes and quasi-liquid molecules rendered semi-transparently. Basal and prismatic facets are evident. Also evident are beveled facets intersecting the prismatic and basal facets, with well-defined edges. Although the beveled facet has symmetry like that of the prismatic pyramidal facets shown in Fig. 1, it subtends a significantly larger angle with respect to the prismatic plane (28° compared to 14°). Viewed along the crystallographic c-axis (Fig. 7b), the lower prismatic facet is still evident, but the upper one is congested by ice molecules attached to low-z portions of the crystal (off the scale to the left of Fig. 6a). One prismatic edge is clearly in evidence.

In view of the observed stability of prismatic edges even under ablation conditions (Fig. 3), we investigated departures of molecules from the surface of our nanocolumn for possible atomistic edge effects. Figure 8 is a representation of the free-standing nanocolumn highlighting positions of molecules at the closest recorded time step prior to departure from the surface (within 10 ps). The absence of any obvious preference for departure from edges or vertices suggests that sublimation is controlled by dynamics of the quasi-liquid layer, not by the hexagonal cross section of the underlying ice.

Departure rates from the free-standing nanocolumn, along with results for the pris-

matic slab described in Sect. 2.2, and of a basal slab reported by Neshyba et al. (2009), are displayed in Table 1. We have not undertaken a thorough analysis of uncertainty in these values, but it is unlikely the uncertainty exceeds ±100 Pa, since a detailed uncertainty analysis of similar calculations of a basal slab yielded ±50 Pa (Neshyba et al., 2009). The vapor pressure of the free-standing nanocolumn is, therefore, significantly greater than that of flat prismatic or basal surfaces under the same conditions.

These findings are contradictory: sublimation is not enhanced at facet edges, but sublimation is enhanced by the existence, underneath the quasi-liquid, of facet edges. It seems likely that the resolution lies in our definition of an edge, i.e. that the effective edge spans a distance >1–2 nm, a significant distance compared to the size of the model. Simulations of longer time or larger cross sectional area are needed to test this explanation.

Finally, we see in the MD simulations no evidence of growth instability suggestive of trans-prismatic strands. Indeed, underneath the quasi-liquid layer the basal and prismatic facets have nearly perfect molecular smoothness. We conclude that trans-prismatic strands originate at a higher level of spatial organization (>10 nm).

4 Discussion

The VP-SEM micrographs presented here bear a certain resemblance to SEM results of ablating ice presented by (Cross, 1968). By producing ice hexagons in such a way that the crystals can be imaged during growth as well as ablation, in a controllable and reversible way, the present technique offers a way to assemble a picture of ice more clearly relevant to atmospheric conditions.

In the MD study of Pereyra and Carignano (2009), it was argued that prismatic edges are atomistically robust. The present results reinforce this idea in several ways. Our MD system differed from that of Pereyra and Carignano (2009) in that a different intermolecular potential was used, and the nanocolumn was free-standing, but atomistically stable prismatic edges persisted anyway. We have, moreover, found other atomistically

stable facet edges, at the intersections of beveled surfaces with basal and prismatic facets. The SEM micrographs presented here provide experimental evidence that prismatic edges are also robust at much larger scales than the molecular: the mesoscopic scale is 10^4 times larger than the atomistic.

In addition to supporting the rough-surface hypothesis, the present results can help refine microphysical representations of cirrus clouds in climate models. First, we submit that different representations (in terms of surface roughness) are needed for clouds that are growing and clouds that are ablating. Ablating crystals are shown here to be much rougher than growing crystals. If cirrus ice crystals exhibit growth and ablation strands like those presented here, it follows that ablating cirrus clouds would be more reflective, gram for gram, than would growing cirrus clouds. Secondly, this work shows that the surfaces of cirrus ice analogues are rough in a trans-prismatic fashion. This symmetry is markedly different from representations currently in use in radiative transfer simulations. For example, Yang et al. (2008b) use a parameterization for surface roughness that has no intrinsic hexagonal symmetry. The present results would be useful in constructing more realistic parameterizations.

Do cirrus ice crystals exhibit surface features such as those seen here? Our crystals are grown on a substrate, not as free particles, and the surrounding gas is mostly water vapor, not air. On the other hand, the present crystals assume a hexagonal shape like cirrus crystals, and exist in a similar range of temperature and supersaturation (Jensen et al., 2005; Krämer et al., 2009). Examination of real cirrus ice in a VP-SEM should resolve this question.

It is tempting to identify the prismatic pyramidal facets observed with VP-SEM with the beveled facets evident in our MD simulations, but unfortunately, the angles do not match: the former subtend a significantly smaller angle (14°) than do the latter (28°). (The MD-observed beveled surface may have more to do with a facet proposed by Goldie et al. (1976) to explain an unusual concentric halo.) Since the observed prismatic pyramidal facets are most prominent during fast growth conditions, they are unlikely to be Wulff-related equilibrium structures such as those reported by Elbaum and

Wettlaufer (1993). On the other hand, we do not exclude the possibility that these facets are associated with kinetic Wulff shapes, as described by phase field theory (Sekerka, 2005).

The methods presented here should be useful in constraining theories of growth that rely on mesoscopic or atomistic arguments. For example, as noted above, the prismatic pyramidal facets evident in our VP-SEM micrographs exhibit ledges and terraces during growth and ablation. It is unclear what relationship these morphological elements have with strands, if any. Such facet-specific distinctions would be relevant to theories of ice crystal growth using the theory of structure-dependent attachment kinetics, which proposes that ice growth on a particular facet depends on the microscopic structure of the facet (Libbrecht, 2003). Also, since ablation strands are dynamically and morphologically distinct from growth strands, we note that a theory of crystal ablation incorporating such morphologies would be useful as a complement to current theories of crystal growth.

5 Summary

Growth and ablation of hexagonal ice prisms are processes mediated by trans-prismatic strands. Collectively, these strands impose a mesoscopic-scale roughness on prismatic surfaces, evident at a wide range of supersaturations. During growth, these strands are spaced 5–10 μm apart, and collectively extend over interiors of prismatic facets more than prismatic edges. During ablation, trans-prismatic strands are characterized by a deepening and wider distribution of separations; collectively, these strands appear first at prismatic edges. Prismatic edges are evident and robust under both growth and ablation conditions. MD simulations suggest that the robustness of prismatic edges, pyramidal prismatic-prismatic edges, and pyramidal prismatic-basal edges, have an atomistic origin. MD studies showed no evidence of trans-prismatic strands at the atomistic level, suggesting that these surface structures originate at a larger spatial scale. Finally, the roughness characteristics presented here could be

used to construct more realistic representations of cirrus clouds in climate models.

Acknowledgements. We thank A. Vallecorsa and R. Bentson for their technical assistance. W.C.P. and R.M.H. were supported by Canfield Research Grants administered through the University of Puget Sound. The authors would like to dedicate this paper to the memory of Stewart Lowther, with whom S.P.N. spent many fruitful hours at an SEM console.

References

Bailey, M. and Hallett, J.: Growth Rates and Habits of Ice Crystals between −20°C and −70°C, J. Atmos. Sci., 61, 514–544, 2004.

Buch, V., Sandler, P., and Sadlej, J.: Simulations of H_2O Solid, Liquid, and Clusters, with an Emphasis on Ferroelectric Ordering Transition in Hexagonal Ice, J. Phys. Chem. B, 102, 8641–8653, 1998.

Buck, A. L.: New equations for computing vapor pressure and enhancement factor, J. Appl. Meteorol., 20, 1527–1532, 1981.

Carignano, M., Shepson, P., and Szleifer, I.: Molecular dynamics simulations of ice growth from supercooled water, Mol. Phys., 103, 2957–2967, 2005.

Cartwright, J. H. E., Escribano, B., and Sainz-Diaz, C. I.: The mesoscale morphologies of ice films: Porous and biomorphic forms of ice under astrophysical conditions, Astrophys. J., 687, 1406–1414, 2008.

Cross, J. D.: Study of the surface of ice with a scanning electron microscope, in: Physics of Ice: Proceedings of the international symposium on physics of ice, edited by: Riehl, N., Bullemer, B., and Engelhardt, H., Plenum, 81–94, 1968.

Elbaum, M. and Wettlaufer, J. S.: Relation of growth and equilibrium crystal shapes, Phys. Rev. E, 48, 3180–3183, 1993.

Erbe, E. F., Rango, A., Foster, J., Josberger, E. G., Pooley, C., and Wergin, W. P.: Collecting, Shipping, Storing, and Imaging Snow Crystals and Ice Grains With Low-Temperature Scanning Electron Microscopy, Microsc. Res. Tech., 62, 19–32, 2003.

Garrett, T. J.: Observational quantification of the optical properties of cirrus cloud: In Light Scattering Reviews, Praxis, edited by: Kokhanovsky, A., Praxis, vol. 3, 2008.

Gerber, H., Takano, Y., Garrett, T. J., and Hobbs, P. V.: Nephelometer Measurements of

the Asymmetry Parameter, Volume Extinction Coefficient, and Backscatter Ratio in Arctic Clouds, J. Atmos. Sci., 57, 3021–3034, 2000.
Goldie, E. C. W., Meaden, G. T., and White, R.: The concentric halo display of 14 April 1974, Weather, 31, 304–311, 1976.
Gravner, J., and Griffeath, D.: Modeling snow-crystal growth: A three-dimensional mesoscopic approach, Phys. Rev E, 79, 011601-1-18, 2009.
Heymsfield, A. J. and Iaquinta, J.: Cirrus crystal terminal velocities, J. Atmos. Sci., 57, 916–938, 2000.
Humphrey, W., Dalke, A., and Schulten, K.: VMD -Visual Molecular Dynamics, J. Molec. Graph., 14, 33–38, 1996.
Jensen, E.J., Smith, J. B., Pfister, L., Pittman, J. V., Weinstock, E. M., Sayres, D. S., Herman, R. L., Troy, R. F., Rosenlof, K., Thompson, T. L., Fridlind, A. M., Hudson, P. K., Cziczo, D. J., Heymsfield, A. J., Schmitt, C., and Wilson, J. C.: Ice supersaturations exceeding 100% at the cold tropical tropopause: implications for cirrus formation and dehydration, Atmos. Chem. Phys., 5, 851–862, 2005, http://www.atmos-chem-phys.net/5/851/2005/.
Krämer, M., Schiller, C., Afchine, A., Bauer, R., Gensch, I., Mangold, A., Schlicht, S., Spelten, N., Sitnikov, N., Borrmann, S., de Reus, M., and Spichtinger, P.: Ice supersaturations and cirrus cloud crystal numbers, Atmos. Chem. Phys., 9, 3505–3522, 2009, http://www.atmos-chem-phys.net/9/3505/2009/.
Lampert, A., Ehrlich, A., Dörnbrack, A., Jourdan, O., Gayet, J.-F., Mioche, G., Shcherbakov, V., Ritter, C., and Wendisch, M.: Microphysical and radiative characterization of a subvisible midlevel Arctic ice cloud by airborne observations – a case study, Atmos. Chem. Phys., 9, 2647–2661, 2009, http://www.atmos-chem-phys.net/9/2647/2009/.
Libbrecht, K. G.: Explaining the formation of thin ice crystal plates with structure-dependent attachment kinetics, J. Cryst. Growth, 258, 168–175, 2003.
Lindahl, E., Hess, B., and van der Spoel, D.: GROMACS 3.0: A package for molecular simulation and trajectory analysis, J. Mol. Model., 7, 306–317, 2001.
Nada, H. and van der Eerden, J. P. J. M.: An intermolecular potential model for the simulation of ice and water near the melting point: A six-site model of H_2O, J. Chem. Phys., 118, 7401–7413, 2003.
Neshyba, S. P, Grenfell, T. C., and Warren S. G.: Representation of a nonspherical ice particle by a collection of independent spheres for scattering and absorption of radiation: 2. Hexagonal columns and plates, J. Geophys. Res., 108, 4448, doi:10.1029/2002JD003302,

2003.
Neshyba, S. P, Nugent, E., Roeselová, M., and Jungwirth, P.: Molecular Dynamics Study of Ice-Vapor Interactions via the Quasi-Liquid Layer, J. Phys. Chem. C, 113, 4597–4604, 2009.
Pereyra, R. G. and Carignano, M. A.: Ice Nanocolumns: A Molecular Dynamics Study, J. Phys. Chem. C, 113, 12699–12705, doi:10.1021/jp903404n, 2009.
Rango, A., Wergin, W. P., Erbe, E. F., and Josberger, E. G.: Snow crystal imaging using scanning electron microscopy: III. Glacier ice, snow and biota, Hydrol. Sci. J., 45, 357–375, 2000.
Saito, Y.: Statistical Physics of Crystal Growth, World Scientific, 192 pp, 1996.
Sekerka, R. F.: Equilibrium and growth shapes of crystals: how do they differ and why should we care?, Cryst. Res. Technol., 40, 291–306, 2005.
Stephens, G. L., Tsay, S. C., Stackhouse, P. W., and Flatau, P. J.: The relevance of the microphysical and radiative properties of cirrus clouds to climate and climate feedback. J. Atmos. Sci., 47, 1742–1753, 1990.
Ulanowski, Z., Hesse, E., Kaye, P. A., and Baran, A. J.: Light scattering by complex ice-analogue crystals, J. Quant. Spectrosc. Radiat. Transfer, 100, 382–392, 2006.
Wood, S. E., Baker, M. B., and Calhoun D.: New model for the vapor growth of hexagonal ice crystals in the atmosphere, J. Geophys Res., 106, 4845–4870, 2001.
Yang, P., Zhang, Z., Kattawar, G. W., Warren, S. G., Baum, B. A., Huang, H.-L., Hu, Y. X., Winker, D., and Iaquinta, J.: Effect of Cavities on the Optical Properties of Bullet Rosettes: Implications for Active and Passive Remote Sensing of Ice Cloud Properties, J. Appl. Meteorol. Clim., 47, 2311–2330, 2008a.
Yang, P., Hong, G., Kattawar, G. W., Minnis, P., and Hu, Y.: Uncertainties Associated With the Surface Texture of Ice Particles in Satellite-Based Retrieval of Cirrus Clouds: Part II-Effect of Particle Surface Roughness on Retrieved Cloud Optical Thickness and Effective Particle Size, IEEE T. Geosci. Remote Sens., 467, 1948–1957, 2008b.
Yang, P. and Liou, K. N.: Single-scattering properties of complex ice crystals in terrestrial atmosphere, Contr. Atmos. Phys. 71, 223–248, 1998.
Zimmermann, F., Ebert, M., Worringen, A., Schutz, L., and Weinbruch, S.: Environmental scanning electron microscopy (ESEM) as a new technique to determine the ice nucleation capability of individual atmospheric aerosol particles, Atmos. Environ., 41, 8219–8227, 2007.

Table 1. MD-derived vapor pressures at 250 K.

System	Interval (ns)	Departures	P_{vap} (Pa)
prismatic slab	58.2	14	130
basal slab	173	37	240±50
free-standing nanocolumn	4.2	31	390

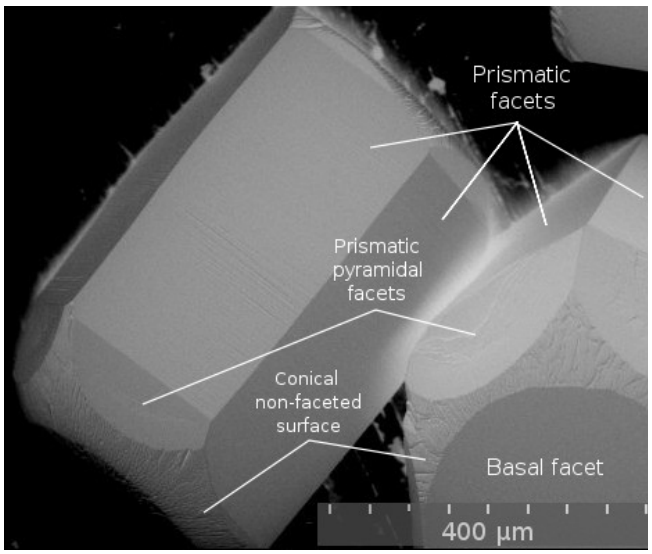

Fig. 1. SEM images of growing ice crystals. Hexagonal ice crystals showing the conical non-faceted (CNF) surface and prismatic pyramidal, prismatic, and basal facets.

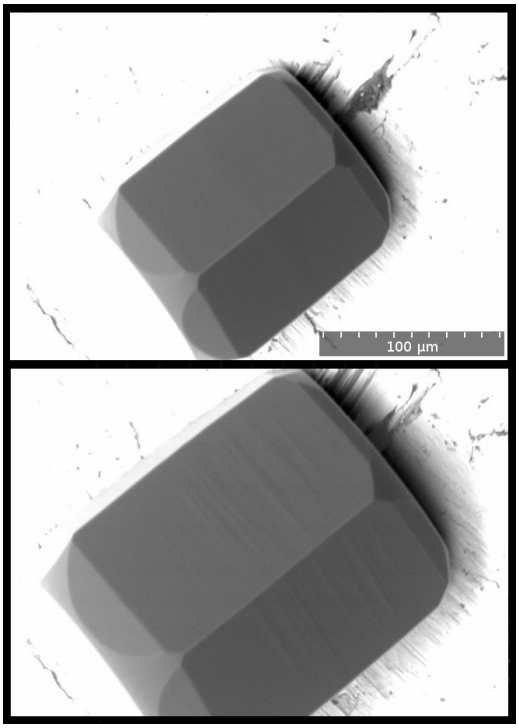

Fig. 2. Hexagonal ice crystal in an early stage of growth. The first micrograph was taken seconds after the crystal was noticed, the second was taken 32 s later.

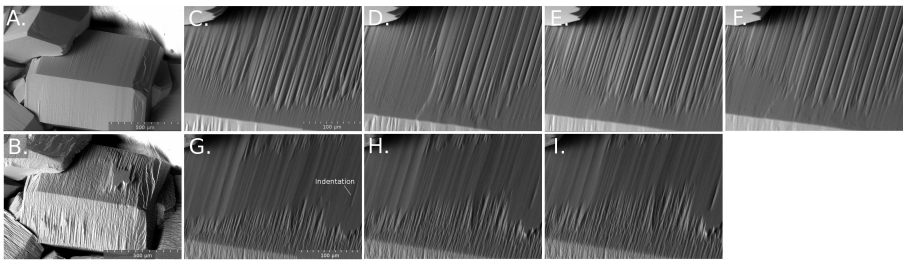

Fig. 3. Growth and ablation of a hexagonal ice crystal. Scale bars in the first image of each series apply to all images in the series. (**A**) Low magnification view of a growing ice crystal. **(B)** View of the same crystal after ∼15 min of ablation conditions. (**C–F**) Higher magnification sequence showing growth at the prismatic edge visible in A, taken at intervals of ∼30 s. **(G–I)** Sequence showing ablation at the same prismatic edge, at intervals of ∼30 s.

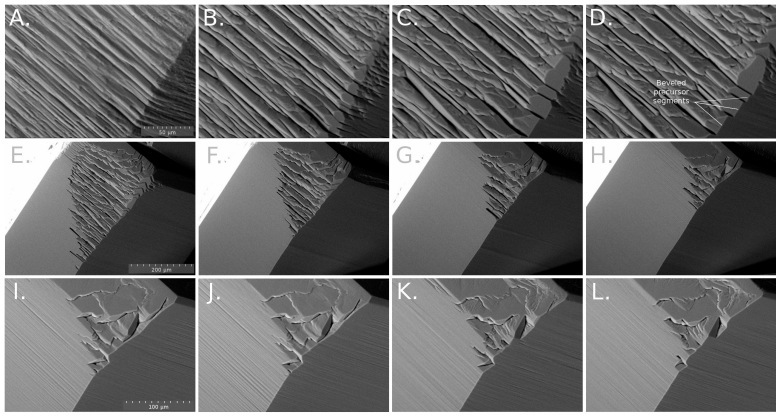

Fig. 4. Re-growth sequences of a previously ablated crystal. Scale bars in the first image of each series apply to all images in the series. (**A–D**) View of the prismatic edge during initial regrowth of an ablated crystal, at intervals of ∼45 s. (**E–H**) Regrowth on the same crystal a few minutes later, at lower magnification, at intervals of ∼90 s. (**I–L**) Final regrowth of the ablated edge, at higher magnification with intervals of ∼45 s.

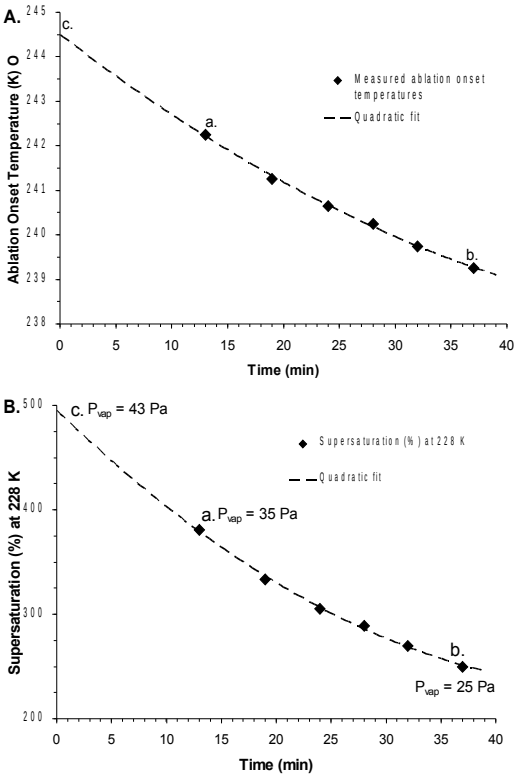

Fig. 5. (**A**) Ablation onset temperature over time for a single SEM session. (**B**) Supersaturation values at the examination stage obtained from Eq. (2), assuming an examination stage temperature of 228 K.

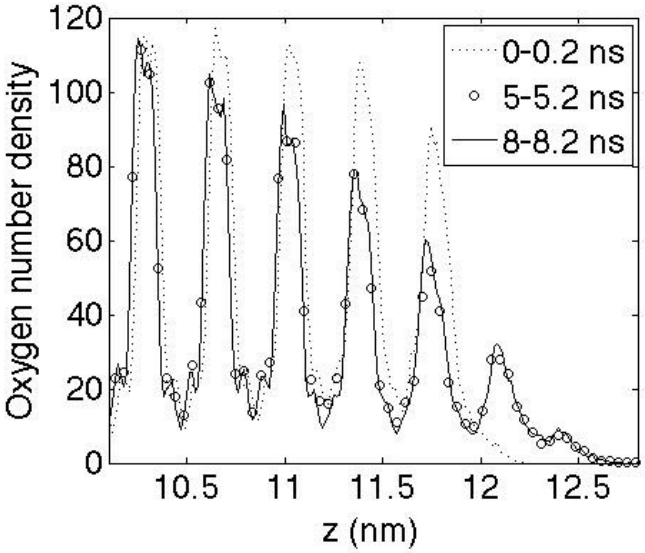

Fig. 6. Integrated number density of oxygen atoms of the free-standing nanocolumn as a function of distance along the crystallographic c-axis (z). Time = 0 refers to the moment at which basal surfaces were exposed to vacuum.

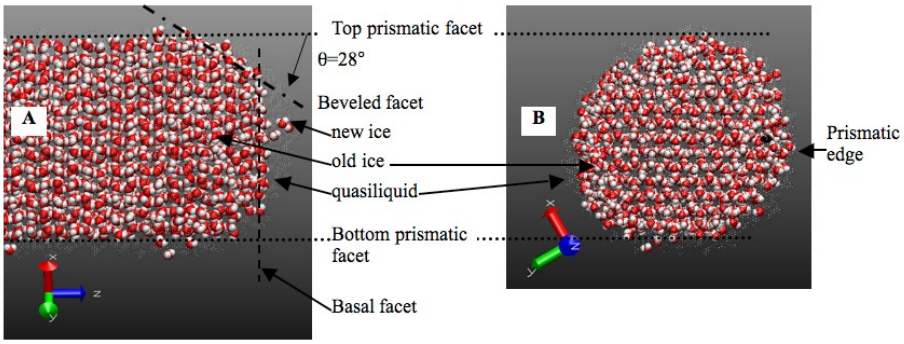

Fig. 7. Representations of a freestanding nanocolumn of 8400 water molecules, simulated by molecular dynamics. **(A)** Configuration 4 ns after exposure of basal surfaces. Ice-like molecules are rendered as solid shapes, others rendered semi-transparently. (**B**) Basal view of (A). "Old ice" points to molecules that existed as ice before exposing the basal surface to vacuum, "new ice" points to molecular positions that became ice-like afterward.

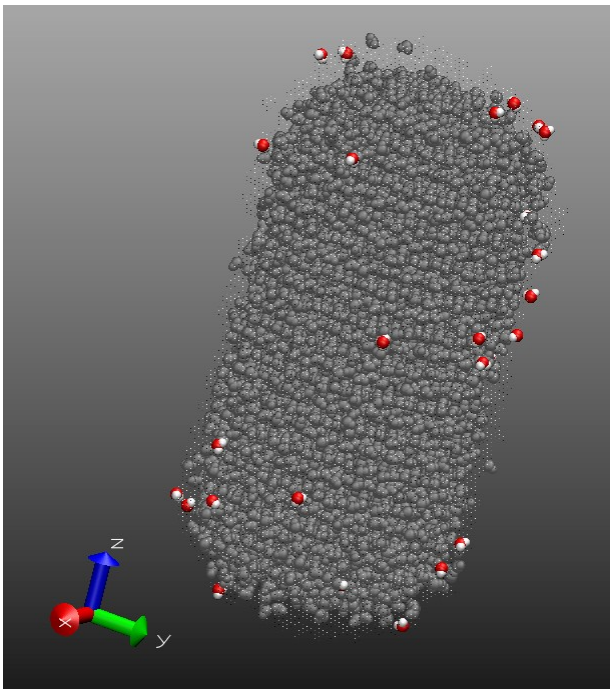

Fig. 8. Free-standing nanocolumn showing the positions of departing (sublimating) water molecules 10 ps or less before departure, over 4 ns simulation time.